buildings

MDPI

Article

Study on Construction Techniques and Key Joints of Giant Arch Suspension Building

Yuenan Jiang [1], Chengcheng Xu [2], Suola Shao [3,*] and Wenping Wu [4]

[1] School of Architectural Engineering, Jinling Institute of Technology, No. 99 Hongjing Road, Nanjing 211169, China; yuenanjiang@jit.edu.cn
[2] College of Civil Engineering and Architecture, Zhejiang University of Water Resources and Electric Power, Xiasha Education Area, Qiantang District, Hangzhou 310018, China; xcc@zuwe.edu.cn
[3] School of Construction Engineering, Zhejiang Sci-Tech University, Xiasha Education Area, Qiantang District, Hangzhou 310018, China
[4] Jiangsu Huning Steel Mechanism Co., Ltd. Xuzhang Road, Yixing 214200, China
* Correspondence: solar_shao@zstu.edu.cn

Abstract

Arch-suspended structures represent a distinctive form of hybrid suspension system. By combining an arch with a suspended floor system, this structural typology leverages the inherent advantages of both components while mitigating the limitations of each when used independently. This synergy effectively reduces peak internal forces and flexural deformations in structural members. Although widely applied in bridge engineering, research on arch-suspended building structures remains scarce. This paper investigates the construction techniques employed for a large-scale arch-suspended building. The stability of temporary support systems during construction is verified, and the mechanical behavior of critical joints—including the composite slab hanging pillar, arch support, and arch roof—is examined through both experimental testing and numerical simulation. The results demonstrate that a partitioned and segmented construction method is feasible for such complex structures. Structural internal forces and deformations can be effectively controlled by installing tubular temporary supports on both sides of the hanging pillars and lattice temporary supports at the base. Step-by-step unloading of these temporary supports ensures their stability throughout the construction process. Furthermore, the welds in the composite slab hanging pillar effectively transfer tensile forces from the middle plate to the side plates, enabling composite action and collaborative load-bearing among the steel plates. When subjected to loads of 2 times and 4.3 times the design load, localized plasticity was observed in the arch support and arch roof, respectively, while the overall structural integrity remained secure. This study provides a valuable reference for the design and construction of innovative long-span building structures, offering insights that can inform the development and practical application of arch-suspended systems in future architectural projects.

Keywords: arch suspension structure; composite slab hanging pillar; temporary support; arch support; arch roof

Check for updates

Academic Editors: Zhen Liu, Jing Luo and Shaojun Zhu

Received: 21 February 2026
Revised: 17 March 2026
Accepted: 22 March 2026
Published: 26 March 2026

Copyright: © 2026 by the authors. Licensee MDPI, Basel, Switzerland. This article is an open access article distributed under the terms and conditions of the Creative Commons Attribution (CC BY) license.

1. Introduction

Suspended buildings represent a structural typology in which roofs or floors are suspended from vertical cores (shafts or towers) [1–3]. Steel cables and suspenders are typically employed to bear the weight of these suspended elements, a configuration that not

capitalizes on the high tensile strength of steel but also enables considerable architectural flexibility. The earliest known suspended structure is the roof of the Lorraine Armory in France, constructed in 1837. With advancements in structural theory and the increasing strength of constructional steel, suspended structures have gained widespread application since the 1950s. To date, more than 20 countries have constructed nearly 100 suspended buildings of various types [4–6].

Considerable research has been conducted on suspended architecture. Goodno et al. [7,8] developed three-dimensional finite element models to analyze the dynamic performance of suspended structures. Luo et al. [9,10] investigated the seismic response of high-rise suspended structures, establishing seismic response equations and deriving parameters such as damping and vibration energy. Zhang et al. [11] examined the load transfer paths, dynamic behavior, and construction process of the Kaohsiung Municipal Library, a suspended structure. Chen et al. [12] evaluated the structural performance of the Jinqiao National Training Center and proposed strengthening measures for its suspension systems. Wang et al. [13] studied the stability of the main structure, substructure, and suspension truss of the Guiyang 201 Building. Tang [14] analyzed the design parameters and seismic performance of a dish-shaped aerial exhibition hall employing a suspended system. Zhang [15] investigated a diagonal brace transfer-truss suspended structure and conducted numerical analyses of its key joints. Yao et al. [16] assessed the seismic performance of a suspended system, determining the optimal arrangement of anti-lateral displacement components based on modal analysis. Yan et al. [17] explored the mechanical characteristics and specialized construction techniques of a vertical tube suspension system. Zeng et al. [18] introduced a flexible tension suspension system and studied its structural behavior under load. Drawing from an engineering case study, the forms and characteristics of bearing and tie components in hybrid suspension structures have also been examined [19]. More recently, Algirdas et al. [20] analyzed the behavior of a combined suspension structural system under symmetric conditions using an innovative approach, discussing force distribution in rigid elements and nodal displacements.

Arch structures offer distinct mechanical advantages: the horizontal thrust at the arch foot, combined with the horizontal component of axial compression, generates a resisting moment that counteracts the overall bending moment, while the vertical component of axial compression resists shear forces. This mechanism effectively controls both bending and shear deformations. Guo [21] investigated the structural behavior and instability mechanisms of steel arches, proposing corresponding calculation methods. José Luis et al. [22] examined the transverse ultimate strength of box-section arches, considering residual stresses and initial transverse deflections, and calculated the ultimate transverse strength for various lengths, section heights, and support conditions. Spoorenberg et al. [23] determined the plastic failure load of circular steel arches through numerical analysis. Cheng [24] studied two-hinged circular arches and evaluated their stable bearing capacity. Zhang [25] analyzed methods for combining arch structures with other structural forms and characterized their morphological features.

Compared to standalone arch structures, arch-suspended systems provide additional mid-span elastic supports for the floor plates through cables and suspenders, effectively reducing both the effective span and peak internal forces. This structural form has been widely adopted in bridge engineering. Lu [26] analyzed the arch ring, main girder, suspenders, and substructure of a half-through steel arch bridge, verifying the ultimate bearing capacity under both persistent and seismic design conditions. He et al. [27] established an arch support model for a steel arch bridge, incorporating material and geometric nonlinearities to analyze stress distribution at the arch foot. Their results indicated that the

average stress at the arch foot remains below the yield stress under the most unfavorable loading conditions.

In recent years, as large-span buildings have become increasingly prevalent, architectural forms have grown more diverse. As a representative long-span structural typology, the arch-suspended building combines the advantages of both arch and suspension systems, offering significant potential for large-span applications [28,29]. Li et al. [30] analyzed the characteristics and applications of arch-suspended structures, providing insights for architectural design.

The foregoing literature review indicates that existing research has largely concentrated on suspension structures and arch structures as independent systems. Although several studies have addressed the morphological design of arch-suspended buildings, investigations into their structural performance under various load conditions, numerical simulation considering complex boundary conditions, joint and connection detailing, as well as construction techniques and control technologies—particularly for multi-story configurations—remain limited. While arch-suspended forms have been explored in bridge engineering, their application and study in building structures are still scarce. To address this research gap, the present study investigates, through a detailed engineering case study, the construction techniques and key joint behavior of a large-scale arch-suspended building. The targeted construction methods, innovative temporary support design and verification, as well as the novel hanging pillar and associated testing approaches, contribute to the originality of this work. The findings are expected to provide valuable references for the design and construction of innovative long-span arch-suspended structures, thereby supporting the advancement and broader application of this structural typology in building engineering.

2. Project Overview

The project is situated at the intersection of Tong'an and Jimei Districts in Xiamen City, China. The total construction floor area is 231,725 m^2, comprising 171,955 m^2 of above-ground space and 59,770 m^2 of underground space. The development consists of three primary buildings. Building 1 is an eight-story office structure rising to a height of 45 m, featuring a large-scale arch-suspended structural system supported by steel-reinforced concrete cores. Buildings 2 and 3 are 24-story tower buildings, each reaching 100 m in height, and employ a core tube-frame structural system. The overall site layout is illustrated in Figure 1.

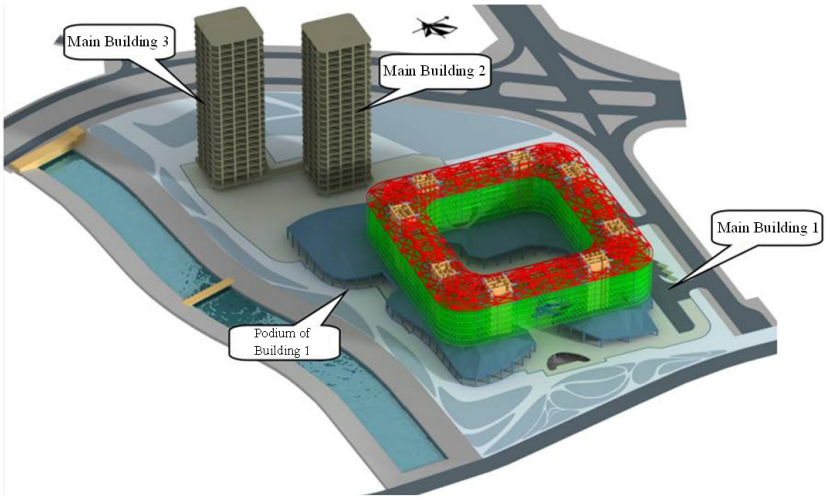


Figure 1. Three-dimensional axonometric drawing of the project.

3. Structural System of Building 1

Building 1 is a square hollow structure, with the outside dimension of 139.2m, inner side dimension of 84.0 m, and the floor width is 27.6 m. The structural system primarily comprises reinforced concrete cores, steel arches, steel horizontal trusses, and composite slab hanging pillars. Two reinforced concrete cores are positioned on each side of the building, with the steel arches supported on the upper portions of these cores, spanning three stories. The arch feet are interconnected by tension cables, forming a self-balancing system. Figure 2 presents the facade of Building 1.

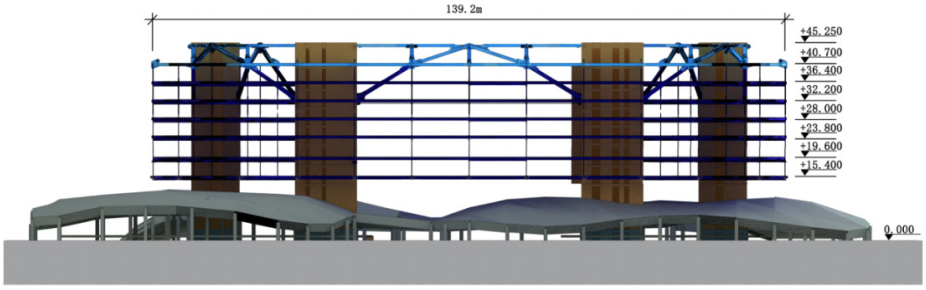


Figure 2. Facade of building 1.

The building incorporates a two-story basement, primarily supported by cruciform and H-shaped steel columns. The core tube has plan dimensions of 12.6 m × 9.6 m and is interconnected by the central main arch and corner oblique arches, as illustrated in Figure 3. The arches are box-section members fabricated from Q460GJC steel, with cross-sectional dimensions of 1000 mm × 800 mm × 80 mm × 100 mm (width × depth × web thickness × flange thickness). The composite slab hanging pillars are also fabricated from Q460GJC steel, with diameters tapering progressively from 325 mm at the top to 150 mm at the bottom. As shown in Figure 4, these hanging pillars transfer floor gravity loads to the steel arches above. The selection of an appropriate construction methodology is therefore critical to ensuring structural safety throughout the erection process.

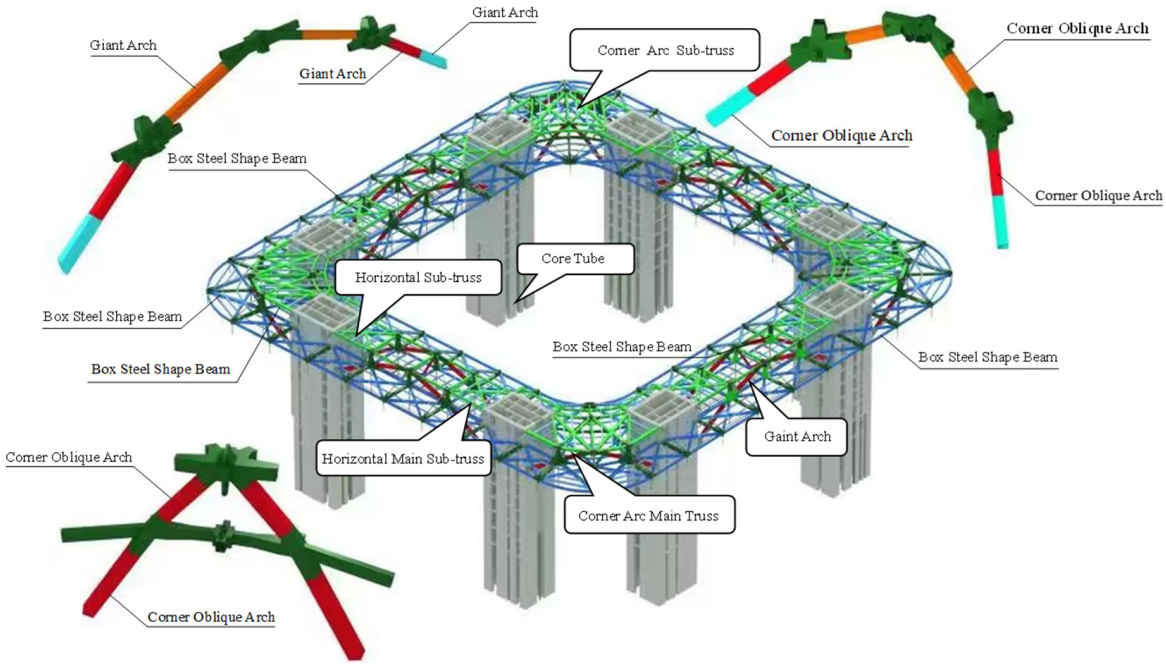


Figure 3. Arch and horizontal truss.

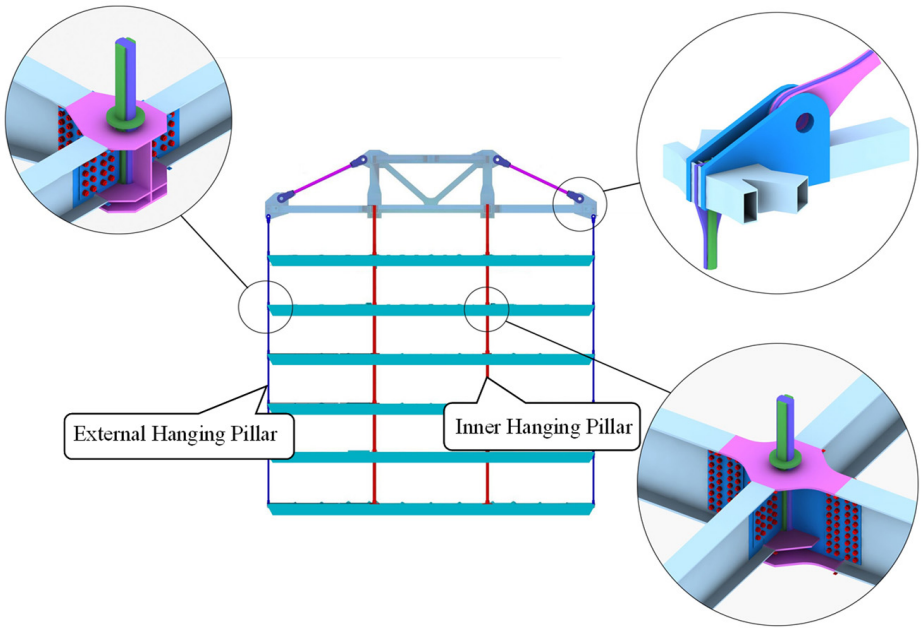


Figure 4. Hanging pillars and joints.

4. Construction Technique and Analysis

The construction of the giant arch-suspended structure presents several significant challenges: (1) The main arch has a maximum span of 50.4 m, while the horizontal trusses feature transverse cantilevers of 9.0 m and corner cantilevers reaching 12.8 m, resulting in substantial deformations during construction; (2) High-strength steel is extensively employed, with many components fabricated from ultra-thick plates—steel plates up to 100 mm in thickness pose considerable welding difficulties; (3) Individual joints in the main arch weigh between 20 t and 29 t, substantially increasing the lifting capacity required from hoisting equipment; (4) The hanging pillars, with diameters ranging from 150 mm to 325 mm, are fabricated by welding three steel plates together. These members cannot support loads during installation and therefore require temporary supports for positioning, which further increases construction complexity.

During the early planning stage, given the challenges of a constrained site, large structural spans, and long cantilevers, multiple construction schemes were discussed. The zoning and segmented construction method was ultimately selected as the most suitable approach and was successfully implemented. Consequently, other construction schemes were not further evaluated during the simulation phase.

4.1. Construction Methodology

Building 1 was constructed in three main stages: underground structure, above-ground structure, and podium, with the above-ground stage being the most critical. For this above-ground stage, a partitioned and segmented construction approach was adopted. The building plan was divided into eight construction partitions. Within each partition, large joints and components were necessarily subdivided into manageable segments for lifting and assembly, whereas smaller joints and components were prefabricated as complete units wherever possible to minimize on-site work. Figures 5 and 6 illustrate the partition layout and component segmentation for Building 1.

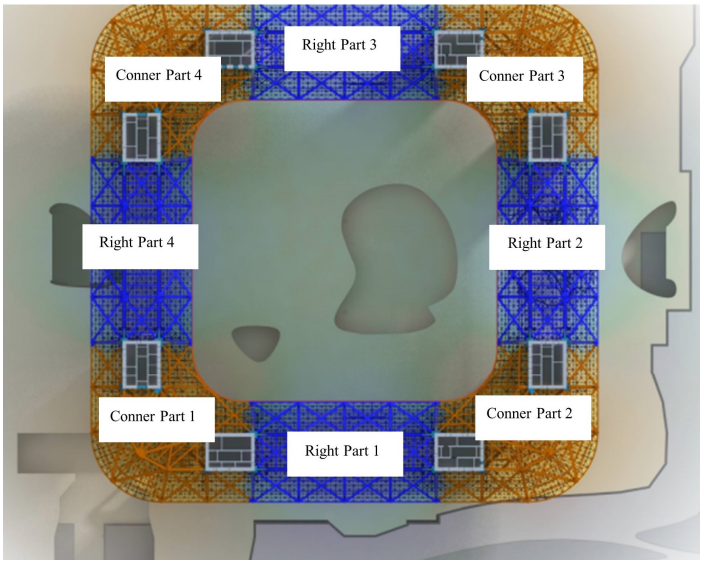
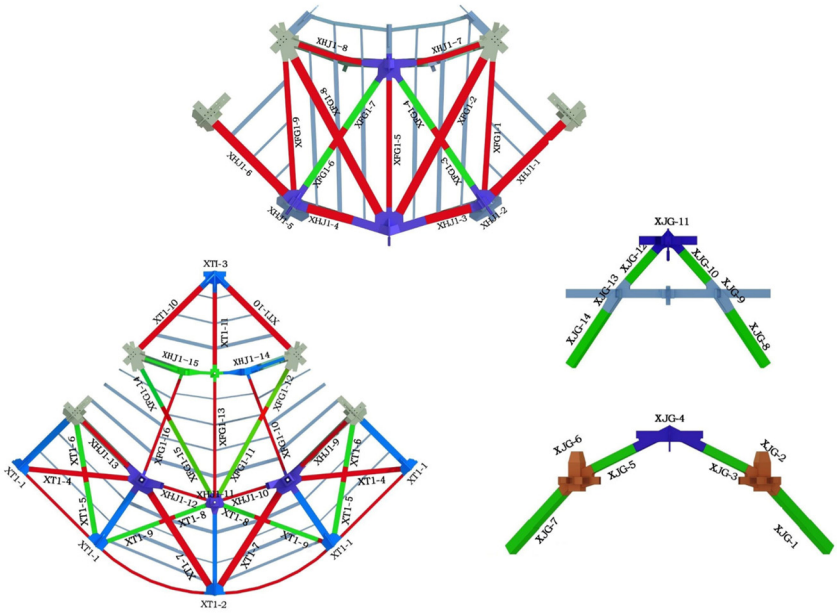
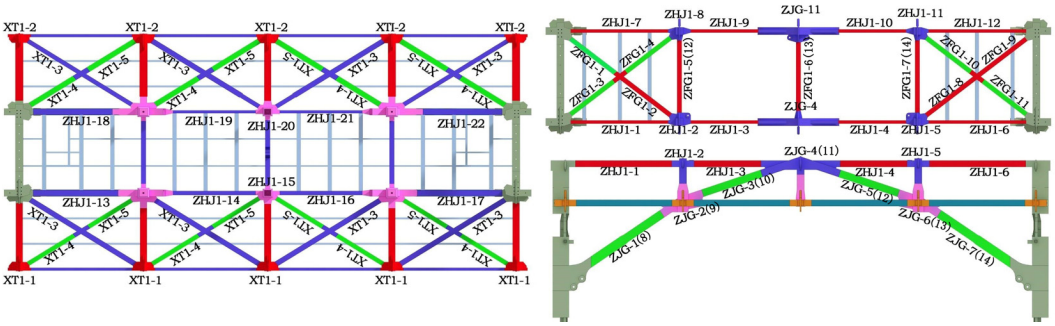


Figure 5. Partitions of Building 1.



(**a**) Corner oblique arches and horizontal trusses



(**b**) Middle giant arch and horizontal trusses

Figure 6. Blocks of the joint and component.

4.2. Construction Procedure

Each partition was constructed following a sequential procedure comprising 17 distinct working conditions:

(1) Erect lattice temporary supports on the basement roof, install steel columns, and pour core tube concrete for the first floor;
(2) Install steel columns and pour core tube concrete for the second floor;
(3) Install steel beams for the second floor, lift the hanging pillars between the second and third floors, and secure them in position using temporary supports;
(4) Install steel columns and pour core tube concrete for the third floor;
(5) Install steel beams for the third floor and place steel floor decks for the second floor;
(6) Lift the hanging pillars between the third and fourth floors and secure them with temporary supports;
(7) Progressively install steel columns for the core tube up to the eighth floor;
(8) Erect the arches spanning between the sixth and eighth floors;
(9) Apply tension to the arch foot cables to 30% of the final design tension;
(10) Pour core tube concrete for the top floor;
(11) Install horizontal trusses outside the connection area and erect the arches between the eighth floor and the roof;
(12) Increase cable tension to 70% of the design value;
(13) After the top floor core tube concrete reaches design strength, install the horizontal trusses within the core tube connection area;
(14) Apply the full design tension (100%) to the cables;
(15) Partially unload the lattice supports and steel pipe supports for the hanging pillars;
(16) Remove most of the lattice supports and steel pipe supports for the hanging pillars;
(17) Completely remove all lattice supports and steel pipe supports for the hanging pillars.

4.3. Simulation Analysis of Construction Process

Internal forces and displacements within the structure continuously evolve throughout the construction process. In this study, the construction sequence was simulated using Midas/GEN (2019) software [31], with all 17 working conditions analyzed in the numerical model. In the model, the reinforced concrete core is simulated using wall elements, the floor slabs using plate elements, and the beams and columns using beam elements. Fixed constraints are applied at the base of the core tube, while hinged constraints are assigned to both the base and top of the temporary supports. Steel beams and columns are modeled in accordance with the design drawings. The cables are connected to the main structure via hinged constraints, modeled using cable elements, and their pre-tension force is simulated by applying equivalent loads. During construction simulation, both self-weight and cable forces are considered. The self-weight is automatically generated by the software, and the weight coefficient is adjusted to ensure consistency with the actual structure. Structural components are grouped according to the construction sequence and are progressively activated in the model to reflect the actual erection process.

Table 1 summarizes the maximum stresses, deformations, and maximum axial forces in the temporary supports for each working condition.

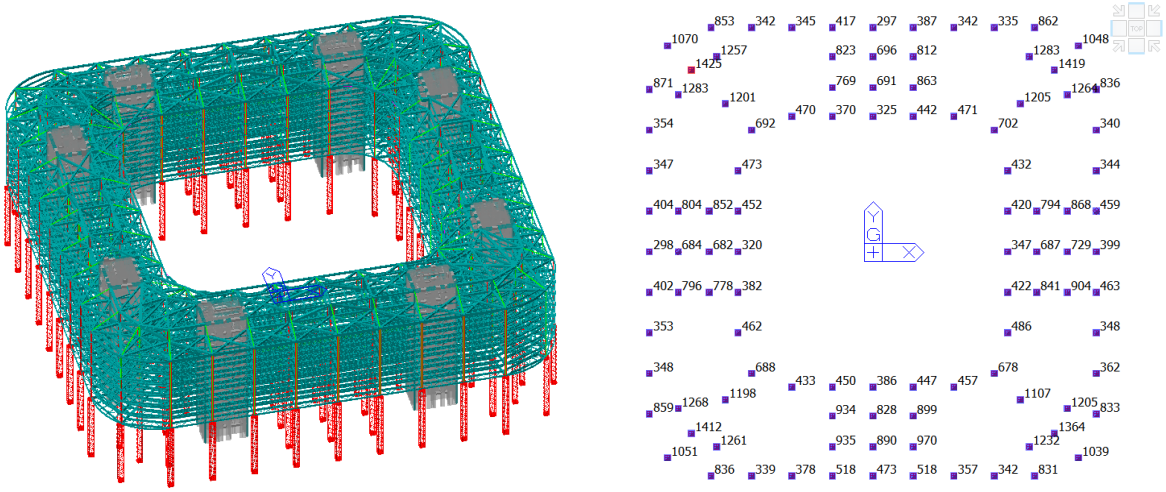
It can be observed from Table 1 that the maximum axial force in the temporary supports occurs under working condition 14. During the support unloading process, significant stresses and deformations develop in the structure; the corresponding simulation results are presented in Figures 7–9.

According to Table 1 and Figures 6–9, the maximum structural deformation is 27 mm, which occurs at the intersection of trusses XFG1-6 and XFG1-7 in corner partition 3, where the total truss length is 10.3 m. The maximum deformation and stress can be verified as follows:

$$27\ mm < 10300/250 = 41.2\ mm,\ 150\ MPa < 270\ MPa$$

Table 1. Maximum value in each working condition.

Construction Procedure	Working Condition	Deformation (mm)	Stress (MPa)	Axial Pressure in Support (kN)
1	cs1	1	−3	77
2	cs2	1	−4	77
3	cs3	3	15	221
4	cs4	3	15	220
5	cs5	4	17	302
6	cs6	4	−21	332
7	cs7	5	−29	436
8	cs8	6	−34	540
9	cs9	6	−35	596
10	cs10	8	44	830
11	cs11	8	44	830
12	cs12	10	47	921
13	cs13	13	−122	1389
14	cs14	15	−148	1425
15	xz1	23	−150	1377
16	xz2	27	139	491
17	xz3	27	139	

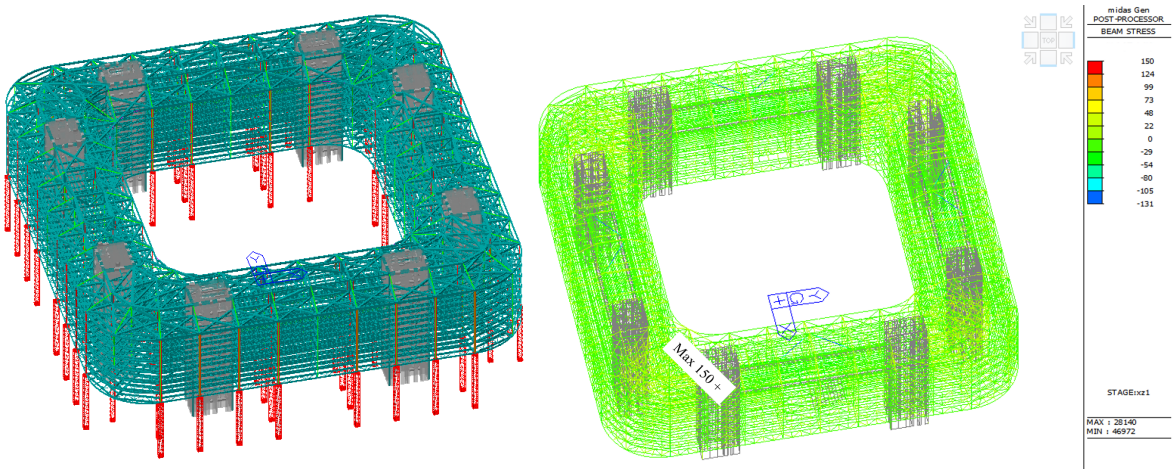


(**a**) Construction model (**b**) Temporary support force (kN)

Figure 7. Simulation results of cs 14.

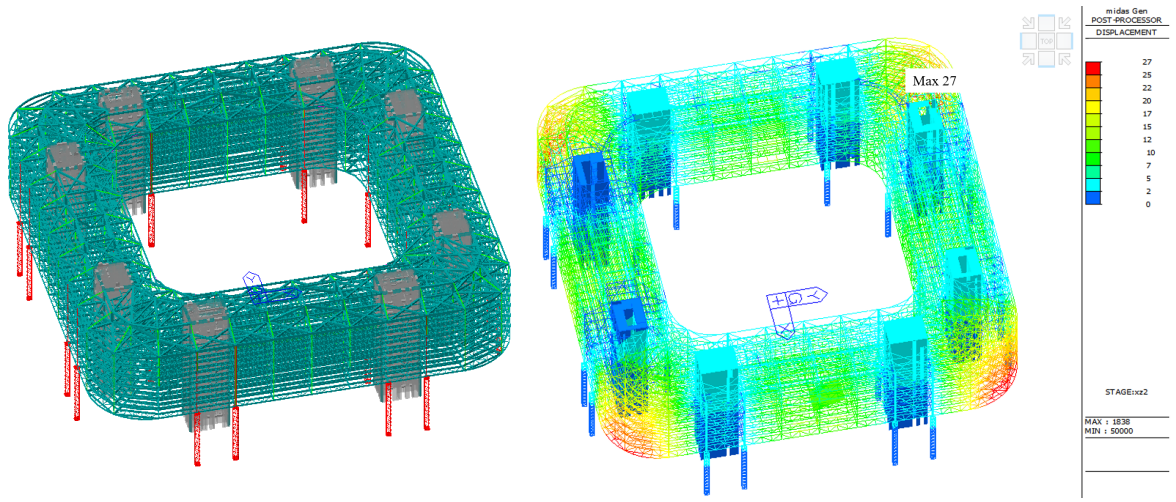
The steel beams are fabricated from Q345B steel, which has a design strength of 270 MPa [32]. Thus, the maximum stress and deformation occurring throughout the construction process comply with the specifications outlined in [32].

It should be noted that the numerical model did not explicitly account for construction tolerances, geometric imperfections, or potential misalignments. This simplification is justified by the construction method adopted: a sectional and zoning symmetrical approach with components and joints prefabricated in the factory to ensure dimensional accuracy. This process significantly minimized geometric imperfections and potential misalignments. Therefore, the influence of these factors on the structural response was considered negligible and was not incorporated into the model.



(**a**) Construction model (**b**) Structural Stress (MPa)

Figure 8. Simulation results of xz 1.



(**a**) Construction model (**b**) Structural deformation (mm)

Figure 9. Simulation results of unloading xz 2.

4.4. Stability Analysis of Temporary Supports

Temporary supports play a critical role in construction safety [33,34]. Three types of temporary supports were employed in this project. The first type consists of 104 lattice temporary supports installed on the basement roof to support the hanging pillars. Each lattice support has a height of 15.4 m and a cross-section of 1.5 m × 1.5 m. The limb members are fabricated from ϕ180 × 8 steel pipes, while the batten members are ϕ102 × 6 steel pipes, with a batten spacing of 1.6 m. The second type comprises 836 tubular steel supports of ϕ245 × 10, used to secure the hanging pillars between the second and sixth floors. The third type consists of 496 tubular steel supports of ϕ180 × 8, employed to fix the hanging pillars from the sixth floor to the roof. These tubular supports have a height of 4.2 m and are fabricated from Q345B steel.

All temporary supports are hinged at both ends. The circular tube supports are arranged symmetrically on each side of the hanging column, with their bottoms welded to gusset plates and tops securely tightened against the formwork; second-order effects were not considered for these supports. In contrast, the lattice supports were designed as cantilever members accounting for second-order effects, with an effective length factor of 2.0 adopted in the stability analysis.

Gravity loads from the main structure are transferred to distribution beams at the top of the temporary supports, which then transmit the forces to the support columns. While hinged constraints are applied at both ends of the temporary supports, the effective length factor for the lattice supports is determined based on a sway frame model to account for second-order effects. Accordingly, the lattice temporary support is idealized as a cantilever member for stability verification.

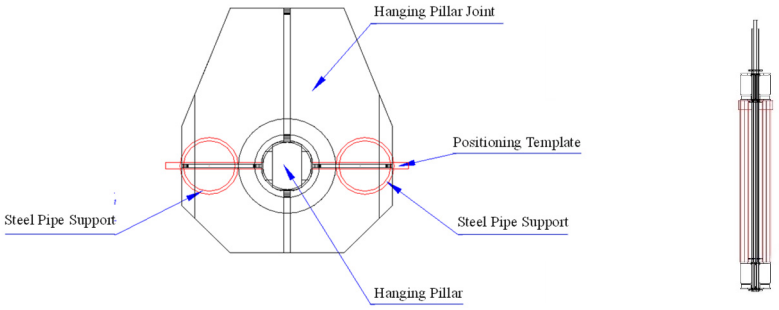
Due to most steel components installed at elevated heights, the stability of temporary support is essential.

4.4.1. Stability Verification of Tubular Steel Supports

According to Table 1 and Figure 10, the maximum axial force in the temporary supports is 1425 kN, with each hanging pillar being secured by two tubular steel supports. The cross-sectional area of each tubular support is A = 7383 mm^2, and the radius of gyration is i = 83.2 mm. Based on an effective buckling length of l_0 = 4200 mm, the slenderness ratio can be determined as follows [32]:

$$\lambda = \frac{l_0}{i} = \frac{4200}{83.2} = 50.48 < [150]$$

And ϕ = 0.796, $\frac{N}{\phi Af} = \frac{(1425/2)\times 1000}{0.796\times 7383\times 305} = 0.4 < 1.0$, which meets the requirement of code [32].



(**a**) Floor view (**b**) Elevation view

Figure 10. Steel pipe support.

4.4.2. Stability Verification of Lattice Temporary Supports

(1) Overall stability

The lattice temporary support is configured as a laced built-up column. The limb members consist of ϕ180 × 8 steel pipes, while the batten members are ϕ102 × 6 steel pipes. The sectional properties of both limb and batten members can be obtained according to the relevant specifications [32].

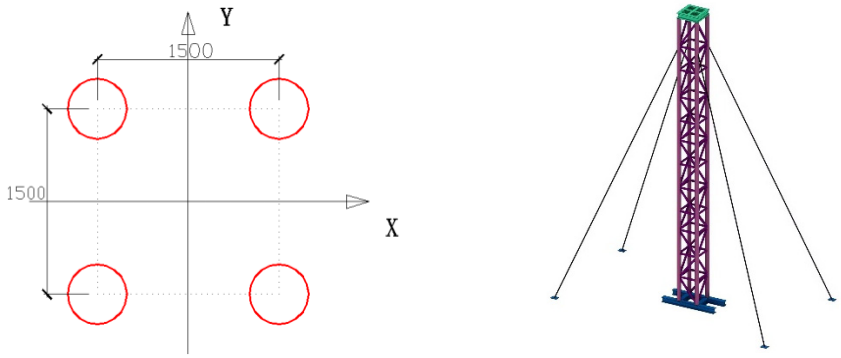
$$A_1 = 43.23\ cm^2,\ I_1 = 1602\ cm^4,\ A_2 = 18.10\ cm^2,\ I_2 = 209.28\ cm^4.$$

According to Figure 11, both axes are imaginary axes and the slenderness ratio must be converted [32].

$$\lambda_{ox} = \sqrt{\lambda_x^2 + 27\frac{A}{A_{1x}}},\ \lambda_{oy} = \sqrt{\lambda_y^2 + 27\frac{A}{A_{1y}}}$$

$$I_x = 4\left[I_1 + A\left(\frac{b}{2}\right)^2\right] = 4\times\left[1602\times 10^4 + 43.23\times 10^2\times\left(\frac{1500}{2}\right)^2\right] = 9.73\times 10^9\ mm^4$$

$$i_x = \sqrt{\frac{I_x}{A}} = \sqrt{\frac{9.73 \times 10^9}{4 \times 43.23 \times 10^2}} = 750\ mm$$



(**a**) Plan sheet (**b**) Elevation map

Figure 11. Lattice temporary support.

Based on the above analysis, the effective length factor of the lattice temporary supports is 2 and the slenderness ratio and the equivalent slenderness ratio can be determined in accordance with the relevant specifications [32].

$$\lambda_x = \mu l / i_x = 2 \times 14.5 \times 10^3 / 750 = 38.67$$

$$\lambda_{0x} = \sqrt{\lambda_x^2 + 27\frac{A}{A_{1x}}} = \sqrt{38.67^2 + 27\frac{4 \times 43.23}{2 \times 18.1}} = 40.3$$

$$\phi = 0.863,\ \frac{N}{\phi A f} = \frac{1425 \times 10^3}{0.863 \times 4 \times 43.23 \times 10^2 \times 305} = 0.31 < 1.0$$

Due to symmetry, the calculation results in the Y-direction are identical, confirming that the overall stability of the lattice support satisfies the code requirements [32].

(2) Limb stability

According to the cross-sectional area and inertia moment of the limb, the rotation radius and slenderness ratio can be calculated [32].

Based on the cross-sectional area and moment of inertia of the limb members, the radius of gyration and corresponding slenderness ratio can be calculated according to the specifications [32].

$$i = 60.9\ mm$$

$$\lambda = \frac{1600}{60.9} = 26.3 < [\lambda] = 150$$

$$\phi = 0.93,\ \frac{N_1}{\phi A_1 f} = \frac{(1425/4) \times 10^3}{0.93 \times 43.23 \times 10^2 \times 305} = 0.29 < 1.0$$

The limbs of the lattice column are also stable [32].

5. Testing of Key Joints

Building 1 employs an arch-suspended structural system in which the hanging pillars transfer floor loads to the arches, and the arches subsequently transmit these loads to the core tubes. To ensure structural safety, experimental testing and numerical simulation were conducted on three critical joint types: the composite slab hanging pillar, the arch support, and the arch roof.

To address the inherent differences between scaled model tests and full-scale prototypes—particularly in welding behavior, residual stress distribution, and local buckling or stress diffusion characteristics—the following measures were implemented to minimize scale effects. The 1:4 scale ratio was selected based on test space, equipment capacity, and measurement accuracy, ensuring both similarity and feasibility. Geometric dimensions were scaled down while maintaining identical materials, loading points, and loading methods as the prototype. Boundary conditions were carefully replicated, stress concentrations were avoided, and high-precision strain gauges were densely arranged in critical regions with graded loading applied to reduce measurement errors. Numerical simulations using ABAQUS 2019 were also conducted to verify consistency in stress distribution, displacement, and stiffness between the test and model results. Through these comprehensive measures—including optimized welding processes, controlled buckling conditions, and refined numerical simulations—the scaled models successfully exhibited the same failure modes as the prototype.

5.1. In-Plane Pure Shear Testing of Composite Slab Hanging Pillar

The hanging pillars, with diameters ranging from 150 mm to 325 mm, are fabricated from Q460GJD steel. Each pillar is composed of three steel plates: the side plates have two adjacent corners trimmed, while the middle plate has all four corners trimmed. The side plates and middle plate are connected using filet welds, with the side plates overlapping the middle plate to form an approximately circular cross-section, as illustrated in Figure 12.

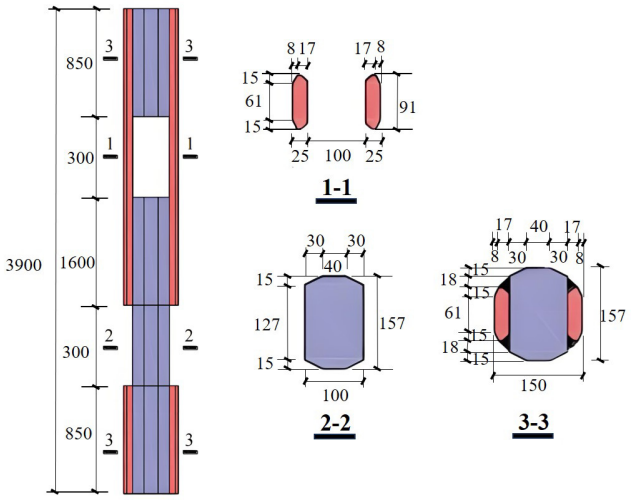


Figure 12. Specimen of D-200.

To investigate the load transfer and cooperative behavior among the individual steel plates, an in-plane pure shear model test was conducted. A composite slab hanging pillar specimen with a diameter of 200 mm and a length of 3900 mm was selected for testing. At one end of the specimen, the side plates were cut away; at the opposite end, the middle plate was cut away, with a cut length of 300 mm in both cases. The test specimen is shown in Figure 12.

5.1.1. Loading Setup and Instrumentation of Composite Slab Hanging Pillar

The loading configuration is illustrated in Figure 13. Both ends of the hanging pillar specimen were welded to loading steel beams, which were equipped with transverse stiffeners to prevent web buckling under concentrated loads. The specimen was positioned on a support table and loaded synchronously using two 400 t hydraulic jacks. Prior to formal testing, three cycles of preloading and unloading were performed, with each preload

stage applying 50 t. During the formal test, load was applied incrementally up to 500 t (the predetermined target load) or until weld failure occurred. To allow for full deformation development, test data were recorded after a 5 min hold at each load increment.

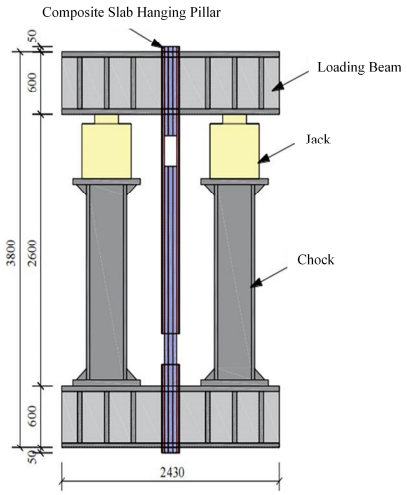
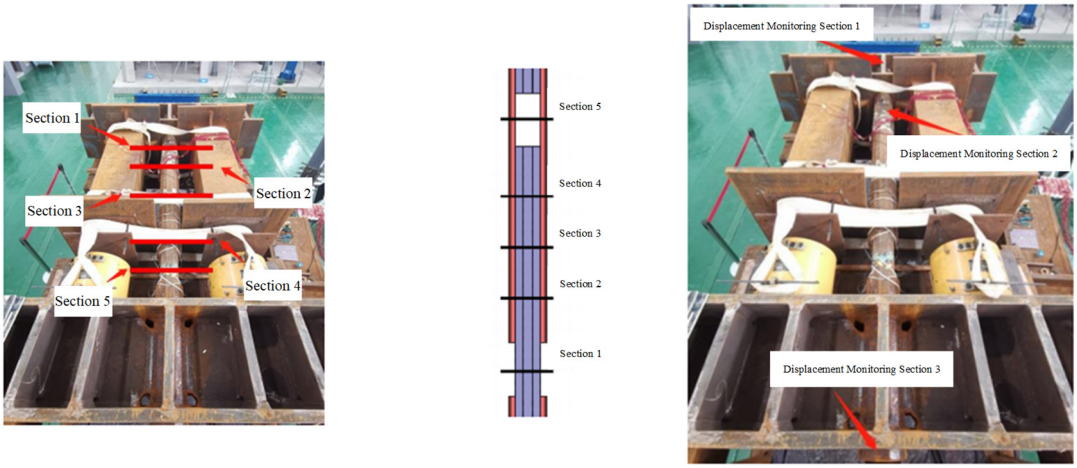


Figure 13. Test loading device.

Figure 14 shows the instrumentation layout. Five strain monitoring sections were established along the specimen to measure strains under in-plane pure shear loading. In this paper, "sections" denote the markings in the figures, not the sections of the article. As shown in Figure 14, sections 1 and 5 monitored strains at the side plate truncation and middle plate truncation, respectively, while Sections 2~4 measured strains in the middle region of the pillar. Each section was instrumented with 4 to 6 strain gauges. Additionally, one displacement transducer was positioned at the end of the hanging pillar, and two displacement transducers were installed at mid-length. All strain and displacement data were automatically recorded using a DH3816N static stress–strain test and analysis system.



(**a**) Strain monitoring sections (**b**) Displacement monitoring points

Figure 14. Monitoring locations.

5.1.2. Model Test Result of Composite Slab Hanging Pillar

Following the test, the maximum and minimum principal stresses at each monitoring point were calculated from the measured strains. The maximum stress was observed at Section 5, where the maximum principal stress at one monitoring point reached 549.98 MPa, exceeding the yield strength of Q460GJC steel. However, all other monitoring points exhib-

ited stresses below 460 MPa, indicating elastic behavior. No significant plastic deformation was observed at the middle plate truncation, and no visible damage to the welds was detected, as shown in Figure 15.

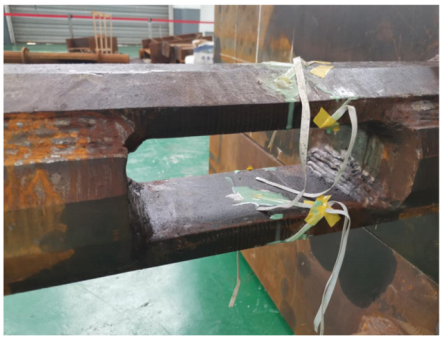


Figure 15. Photo of section 5 after test.

5.1.3. Simulation Result

Numerical simulation of the composite slab hanging pillar was performed using ABAQUS software [35], with the simulation results presented in Figure 16. An ideal elastic-plastic material model was adopted. The side plates, middle plate, and loading beams were modeled using solid elements with type C3D8R. Connections between the steel plates, as well as between the hanging pillar and loading beams, were modeled using tie constraints. To prevent displacement of the loading apparatus, translational constraints were applied to the loading beams in the X and Y directions, with loading applied solely in the Z direction up to 800 t.

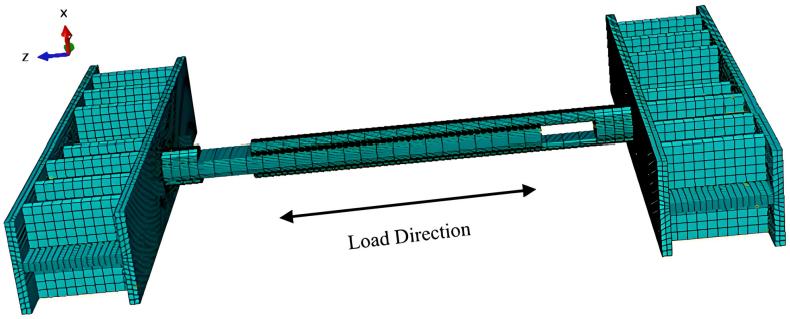


Figure 16. Finite element model of composite slab hanging pillar.

Figure 17 compares the simulation results with the experimental measurements. Good agreement between the numerical and experimental results is evident. The load–displacement curve exhibits no significant change prior to 500 t, indicating that the hanging pillar remains in an elastic state within this range. Due to slight eccentricity during experimental loading, the initial stiffness of the composite slab hanging pillar is somewhat lower than that predicted by the simulation. However, after the simulated load exceeds 600 t, the stiffness begins to decrease, and the axial displacement intensifies. Figures 18 and 19 present stress contour plots of the specimen at a load of 800 t.

As shown in the figures, stress concentrations are clearly visible at the middle plate truncation. In Figure 19a, the maximum stress at the side plate truncation is approximately 355.4 MPa. In Figure 19b, the maximum stress at the middle plate truncation reaches 460 MPa in the numerical simulation, which is lower than the experimental value of 549.98 MPa. This discrepancy arises because numerical simulations cannot fully capture the stress amplification induced by initial geometric imperfections and local force transmission distortions present in the physical test. In Figure 19c, weld stresses are observed to diffuse from both side plates toward the middle plate, with the plastic zone expanding as the load

increases. At a load of approximately 800 t, the diffusion length of yield stress along the weld at the middle plate truncation reaches about 350 mm, compared to approximately 150 mm at the side plate truncation. In Figure 19d, the maximum stress in the loading beam occurs at the weld connection with the specimen; however, the loading beam maintains elastic behavior at 800 t, confirming the adequacy of the loading beam design.

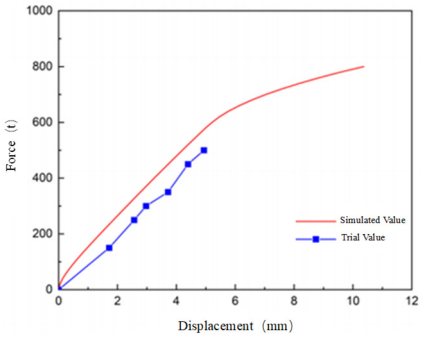


Figure 17. Comparison of the model and simulation result.

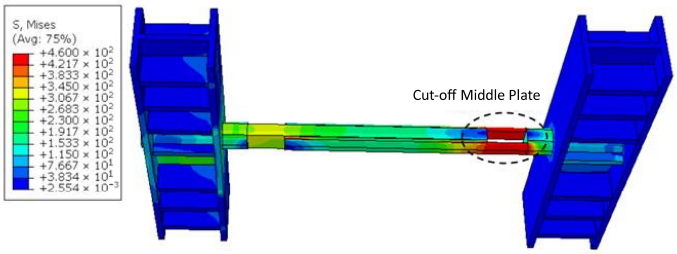
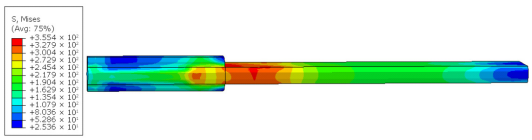
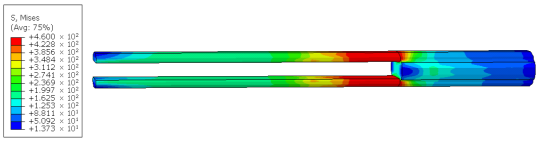


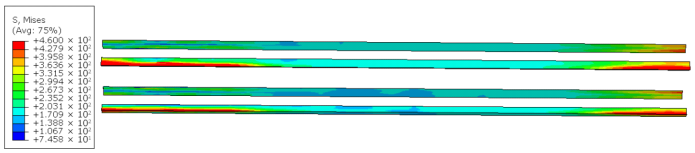
Figure 18. Overall stress of the specimen.



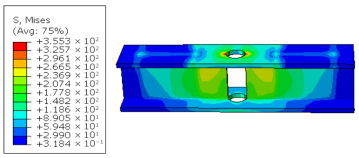
(**a**) Stress contour plot at side plate truncation



(**b**) Stress contour plot at middle plate truncation



(**c**) Stress contour plot of the weld



(**d**) Stress contour plot of the load beam

Figure 19. Stress contour plot in each part.

The simulation results indicate that the specimen exhibits no significant plastic deformation under a load of 500 t, and the welds remain essentially intact. Local yielding at the middle plate truncation occurs only when the load reaches 800 t. Based on both experimental and numerical results, it can be concluded that the welds in the composite slab hanging pillar effectively transfer tensile forces from the middle plate to the side plates, enabling composite action and collaborative load-bearing among the steel plates.

It should be noted that fatigue and long-term performance were not evaluated in this study. This project is a multi-story office building with a steel arch span of 50.4 m. The site is not located in a seismically active region, with relatively low seismic activity frequency, and the climate is mild, with an average annual temperature of approximately 21.2 °C. Based on an analysis of natural environmental factors, functional usage conditions, and cyclic loads generated by the structure itself or its auxiliary facilities, the probability of fatigue failure is relatively low. Nevertheless, construction monitoring was conducted on critical

steel components during the construction phase by the general contractor, and long-term performance evaluation will be carried out after the building is delivered for service.

5.2. Testing of Arch Support

A 1:4 scale model test was conducted for the arch support, as shown in Figure 20. The arch support assembly consists primarily of a main arch and two tension cables. The main arch has a box section of 250 mm × 200 mm × 20 mm × 25 mm (width × depth × web thickness × flange thickness). The cables are fabricated from high-vanadium material with a diameter of 38 mm and a tensile strength of 1670 MPa. The arch, stiffeners, and steel plates are fabricated from Q460GJC steel.

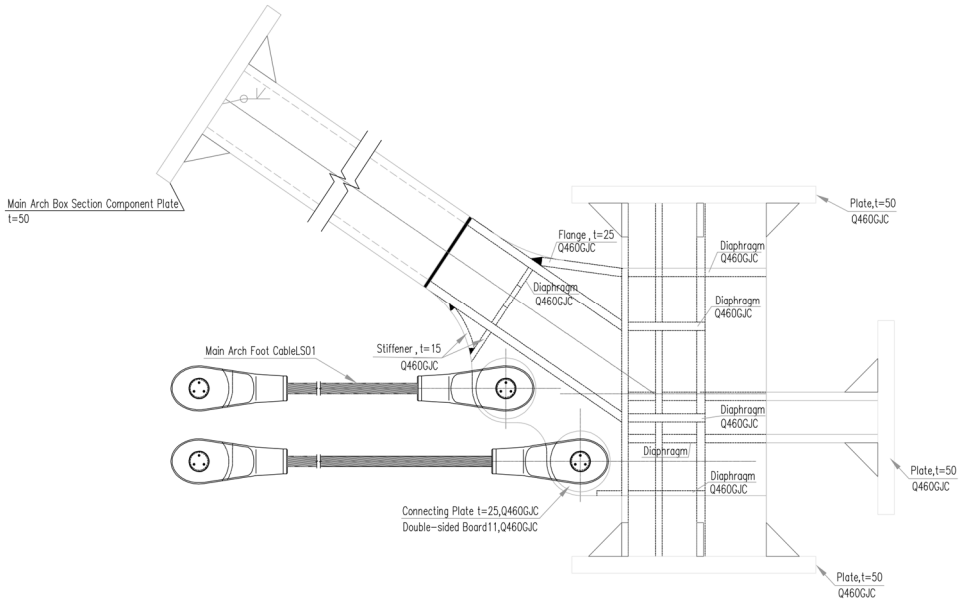
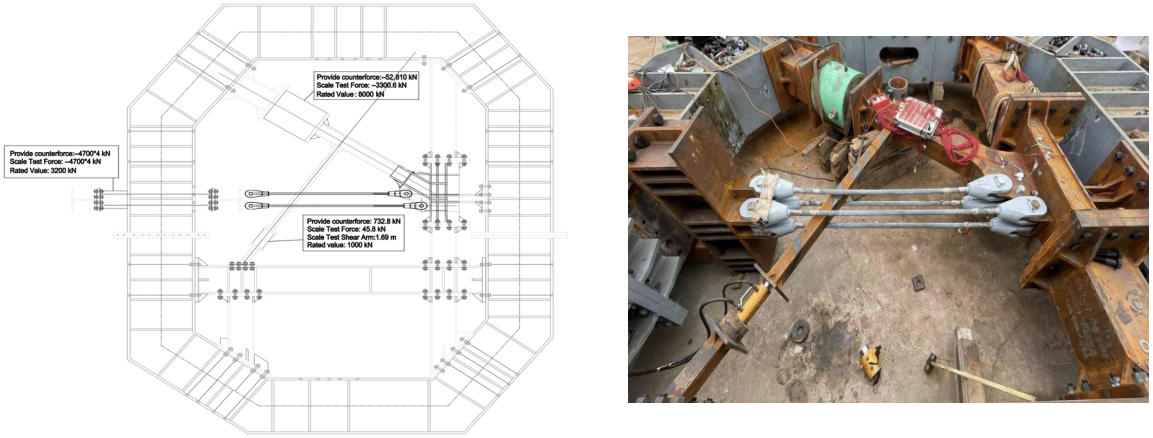


Figure 20. Arch support model.

5.2.1. Loading Setup and Instrumentation of Arch Support

Based on the actual loading conditions, three hydraulic jacks were employed in the model test: an 800 t jack applying axial compression to the main arch, a 400 t jack applying tension to the cables, and a 15 t jack applying lateral load to the main arch. The test setup is illustrated schematically in Figure 21.



(**a**) Model test system (**b**) Loading jack

Figure 21. Model test of arch support.

Load was applied incrementally, with each increment corresponding to one-tenth of the design load. Specifically, each loading step comprised 33 t from the 800 t jack, 11.75 t from the 400 t jack, and 0.46 t from the 15 t jack, applied synchronously. Loading continued until the strain at any monitoring point exceeded the yield strain, at which point the test was terminated.

As shown in Figure 22, several strain monitoring sections (Sections 1–3) were established to measure deformations at the support. Four strain gauges were installed at Sections 1 and 2 to measure axial strains in the main arch, and two strain gauges were placed at Section 3 to measure strains at the joint. Additionally, eight strain rosettes were attached to the front and rear faces of the connection region.

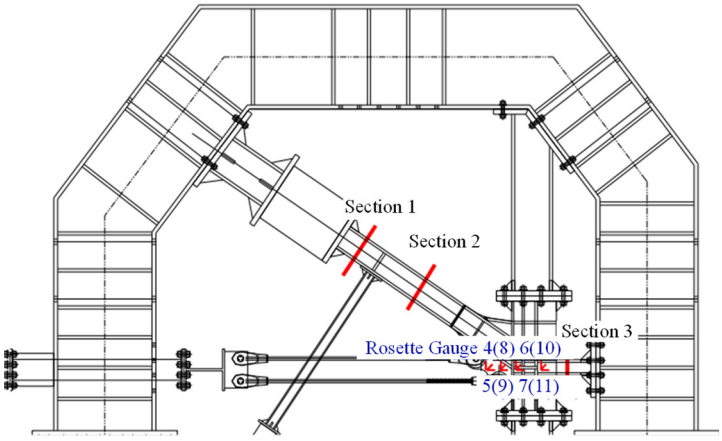


Figure 22. Monitoring sections of arch support.

5.2.2. Model Test Results of Arch Support

When the main arch was loaded to 660 t (twice the design load) and the other jacks were also increased to twice the design load, the strains at measuring points 1–2, 1–3, and 2–4 reached the yield strain of Q460 steel, and the test was terminated. There was no obvious deformation of the component, and no obvious damage to the welds. Table 2 summarizes the measurements from the strain rosettes. Due to instrumentation anomalies, no valid data were obtained from rosette gauges 6 and 9.

Table 2. Summary of the rosette gauges results (unit: $\mu\varepsilon$).

Monitoring Point	The Maximum Principal Strain	The Minimum Principal Strain
Rosette Gauge 4	2636.66	−2958.04
Rosette Gauge 5	1204.32	−1306.68
Rosette Gauge 6	/	/
Rosette Gauge 7	963.90	−1303.58
Rosette Gauge 8	535.04	−1020.71
Rosette Gauge 9	/	/
Rosette Gauge 10	734.13	−1140.28
Rosette Gauge 11	442.31	−1028.87

It can be seen from Table 2 that when loaded to twice the design load, the maximum principal strain of strain gauge 4 is 2636.66, and the minimum principal strain is −2958.04, which exceeded the yield strain of Q460 steel (2233) [32]. By conversion, the maximum principal stress is 490.56 MPa, indicating localized plastic behavior at that location.

5.2.3. Simulation Results of Arch Support

A numerical model of the arch support was developed using ABAQUS software [35], as shown in Figure 23. Solid elements of type C3D8R were employed, and an ideal elastic-plastic material model was adopted. All components were made of Q460 steel, and the constitutive relationship adopts the ideal elastic-plastic model. The component interfaces were modeled using tie constraints. The boundary conditions and loading protocol were consistent with those of the experimental test.

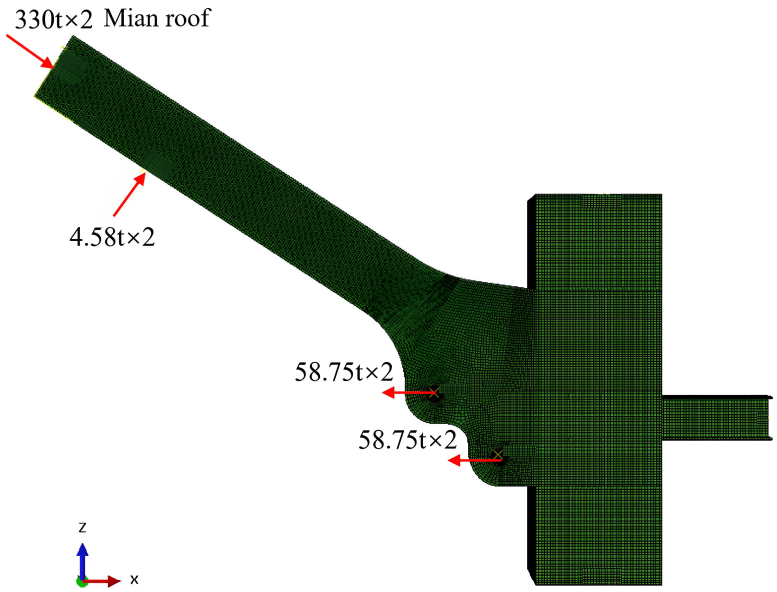


Figure 23. Finite element model of arch support.

Figure 24 presents the numerical simulation results. At a load of 660 t, localized regions of the main arch and the cable connection point reach a maximum stress of 460 MPa, corresponding to the yield strength of the steel. This value is slightly lower than the experimentally observed stress of 490.56 MPa at the same locations. Apart from these localized zones, the remainder of the arch support remains elastic, which is consistent with the experimental observations.

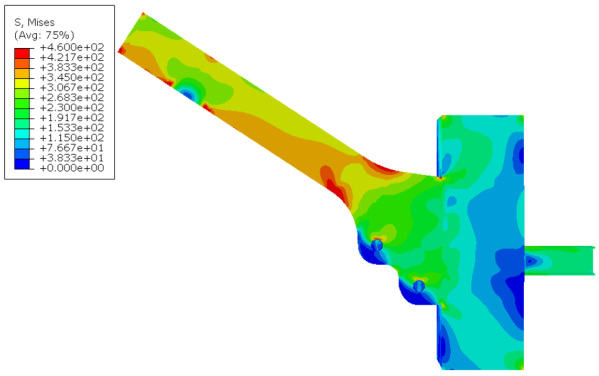


Figure 24. Stress contour plot of arch support.

5.3. Testing of Arch Roof

A 1:4 scale model test was also conducted for the arch roof, as illustrated in Figure 25. The arch roof assembly comprises two main beams, two main arches, and a steel column. The main beams have a section of 175 mm × 87.5 mm × 10 mm × 10 mm, the main arches have a section of 200 mm × 200 mm × 12 mm × 18 mm, and the steel column has a section

of 200 mm × 200 mm × 16 mm × 16 mm. The beam, arch and column are fabricated from Q420GJC steel.

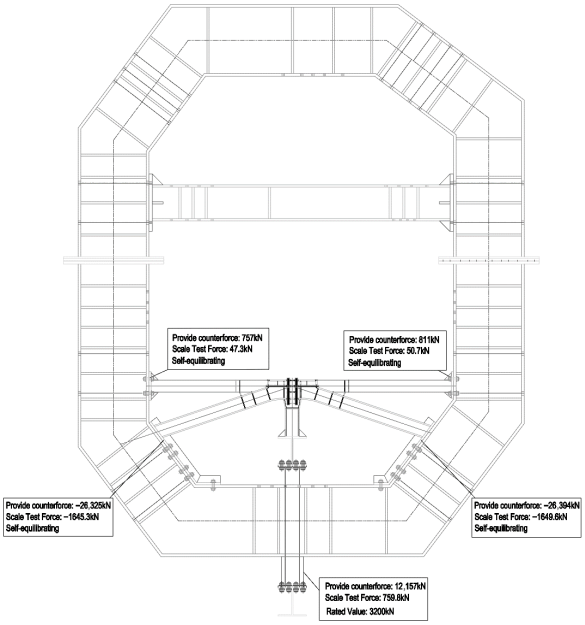


Figure 25. Loading model of arch roof.

5.3.1. Loading Setup and Instrumentation of Acrh Roof

The loading configuration of the arch roof test is shown in Figure 26. The specimen was placed within a reaction frame, with the ends of the main beams and main arches bolted to the frame. The lower end of the steel column was connected to a loading frame consisting of two loading beams and loading columns. Load was applied to this frame using a 400 t hydraulic jack, which transmitted the load to the steel column.



Figure 26. On-site loading.

As shown in Figure 27, several monitoring sections (Sections 1~7) were established for strain measurements. Four strain gauges were installed at Sections 1~5 to measure axial strains in the main components, while six strain rosettes were placed at Sections 6 and 7 to measure principal strains at the connections.

Prior to formal testing, three cycles of preloading and unloading were performed, with each preload stage applying 20 t. Following preloading, the specimen was loaded incrementally in steps of 30 t until the strain at any monitoring point exceeded the yield strain of the steel.

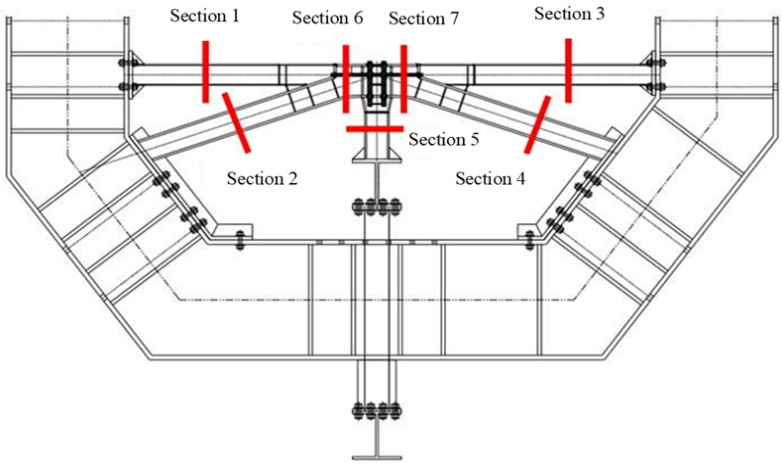


Figure 27. Monitoring sections of arch roof.

5.3.2. Model Test Result of Acrh Roof

The test was terminated when the load reached 330 t, approximately 4.3 times the design load, at which point no visible damage to the specimen was observed. Strains measured at Sections 1~5 (as marked in Figure 27) on the main beams, main arches, and steel column remained below the yield strain of Q420GJC steel (2089 με) [32], indicating that these components can remain elastic throughout the test [36]. The strain rosette measurements at Sections 6 and 7, as indicated in Figure 27, are summarized in Table 3.

Table 3. Results of the strain rosette (unit: $\mu\varepsilon$).

Point Number	Maximum Principal Strain at 330 t	Minimum Principal Strain at 330 t
Rosette Gauge 6-1	3007.07	−1797.49
Rosette Gauge 6-2	1245.27	−7037.22
Rosette Gauge 6-3	2398.82	−3201.1
Rosette Gauge 6-4	10,673.67	−14,302.4
Rosette Gauge 6-5	2233.62	−9725.04
Rosette Gauge 6-6	2369.21	0.25
Rosette Gauge 7-1	4737.34	−5168.50
Rosette Gauge 7-2	15,729.36	−2190.26
Rosette Gauge 7-3	2486.78	−2207.42
Rosette Gauge 7-4	5063.65	−9323.47
Rosette Gauge 7-5	7220.21	−12,053.69
Rosette Gauge 7-6	3086.96	−0.35

As shown in Table 3, the maximum principal strains at most monitoring points exceeded the yield strain of 2233 με [32]. The corresponding average maximum principal stress at Sections 6 and 7, as indicated in Figure 27, is calculated to be 789 MPa, which is significantly higher than the steel's yield strength, indicating that a large portion of the connection joint has entered a plastic state.

5.3.3. Simulation Results of Acrh Roof

A numerical model of the arch roof was developed using ABAQUS software [35], as shown in Figure 28. The connecting plates and flange plates at the junction are made of Q460 steel. The main beams, main arches, and steel columns are made of Q420 steel. An ideal elastoplastic model is adopted, and all components were modeled using solid elements of type C3D8R, with tie constraints employed at all interfaces. Displacement

constraints were applied to the main arches and main beams, and the loading protocol was consistent with that of the experimental test.

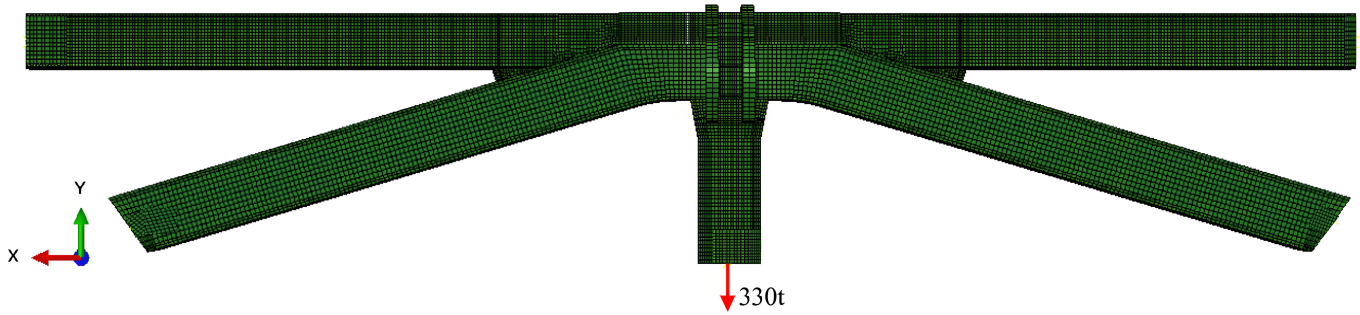


Figure 28. Finite element model of arch roof.

Figure 29 presents the stress contour plot of the arch roof. At a load of 330 t, the maximum stress reaches 471 MPa, exceeding the yield strength of the steel, and a large area of the connection joint has entered a plastic state. Meanwhile, the main beams, main arches, and steel columns remain elastic. These results align closely with the experimental observations.

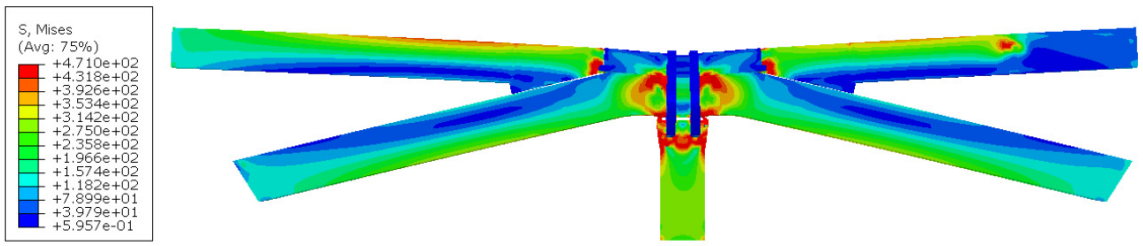


Figure 29. Stress contour plot of arch roof.

The purpose of the joint tests in this project was to verify the ultimate load-bearing performance of the critical joints. According to the relevant code [32], the ultimate bearing capacity of steel joints is required to be 1.5 times the design load. Both the arch springing joint and the arch crown joint satisfied this requirement. Based on the established performance limit and failure criteria—where performance limit represents the upper bound of load-bearing capacity and failure indicates complete loss of force transmission capability—neither joint reached either state. Local buckling observed at the arch springing joint under twice the design load and at the arch crown joint under 4.3 times the design load was considered a reasonable manifestation of plastic development. Accordingly, further investigation into ductility and stress redistribution following local buckling was not pursued, as the joints remained within their intended performance envelope.

6. Conclusions

This paper investigated the construction techniques and key joint behavior of a large-scale arch-suspended building through a comprehensive approach combining construction simulation, theoretical analysis, experimental testing, and finite element modeling. The main conclusions are as follows:

(1) The partitioned and segmented construction method with a 17-step procedure is feasible for long-span arch-suspended structures. Simulation shows the maximum axial force in temporary supports is 1425 kN at installation completion, and peak deformation is 27 mm during unloading—both well within the code-specified limits of 41.2 mm and 150 MPa.

(2) Under the worst-case load of 1425 kN, tubular supports have a slenderness ratio of 50.48 and a stability factor of 0.796, while lattice supports have an equivalent slenderness ratio of 40.3 and a stability factor of 0.863, both meeting code requirements. Batch tensioning of arch foot cables in three stages of 30%, 70%, and 100% and progressive unloading of temporary supports are key to forming the self-balancing system.

(3) The composite slab hanging pillar, consisting of three welded steel plates tapering from 325 mm to 150 mm, exhibits good load-sharing behavior. Under 500 t in-plane pure shear, all but one monitoring point remain below the yield strength of 460 MPa, with no visible weld damage. Local yielding at the middle plate truncation occurs only at 800 t, which is 1.6 times the test load. The welds effectively transfer tensile forces, enabling composite action among the steel plates.

(4) The arch support, comprising a box-section main arch and two high-vanadium cables, remains intact under twice the design load of 660 t. Localized plasticity appears only at the cable connection, where the maximum principal strain reaches 2958.04 με, while all other monitoring points remain elastic. No visible deformation or weld damage confirms the adequacy of the design.

(5) The arch roof assembly, consisting of two main beams, two main arches, and a steel column fabricated from Q420GJC steel, has a high safety margin. At 4.3 times the design load of 330 t, the main components remain elastic with strains below the yield strain of 2089 με, while the connection region yields with a maximum principal strain of 15,729.36 με. These results confirm significant reserve capacity in arch-suspended structures, offering a reference for similar innovative designs.

Findings apply to similar multi-story arch-suspended structures and offer insights for conventional long-span steel projects. Project-specific analysis is needed due to varying arch rise-span ratios. However, theoretical analysis of arch mechanics, cable forces, and arch–pillar interaction is limited. No full-scale joint tests were conducted, and numerical simulations lacked prototype-scale models.

Author Contributions: Y.J.: Conceptualization, Investigation, Software, Writing—original draft, Methodology. C.X.: Project administration, Funding acquisition, Writing—review and editing. S.S.: Writing—review and editing, Supervision, Funding acquisition. W.W.: Visualization, Resources. All authors have read and agreed to the published version of the manuscript.

Funding: This research was funded by Natural Science Foundation of Zhejiang Province [No. LQN26E060009] and the General Research Projects of Zhejiang Provincial Department of Education [No. Y202352639].

Data Availability Statement: Dataset available on request from the authors. Please contact Yuenan Jiang via email at yuenanjiang@jit.edu.cn.

Conflicts of Interest: Author Wenping Wu was employed by the company Jiangsu Huning Steel Mechanism Co., Ltd. The remaining authors declare that the research was conducted in the absence of any commercial or financial relationships that could be construed as a potential conflict of interest.

References

1. Zheng, S.J.; Wang, W.; Jin, H.; Wu, B.H. Development and Application of Large Span Suspension Structures. *Arc. Tec.* **2025**, *56*, 1273–1275.
2. Lehmann, C.R. Multi-storey suspension structures. *Arc. Des.* **1963**, *11*, 530–535.
3. Motro, R. Tensegrity systems and geodesic domes. *Int. J. Space Struct.* **1990**, *3*, 341–351. [CrossRef]
4. Schueller, W. *High-Rise Building Structures*; John Wiley & Sons: Hoboken, NJ, USA, 1977.
5. Zhao, X.A. *Structural Design of Reinforced Concrete High-Rise Buildings*; China Architecture & Building Press: Beijing, China, 1992.
6. Polizovsky, G. *Future Buildings*; Shanghai Science and Technology Press: Shanghai, China, 1982.
7. Goodno, B.J.; Gere, J.M. Earthquake behavior of suspended floor buildings. *J. Struct. Div.* **1976**, *102*, 973–992. [CrossRef]

8. Goodno, B.J.; Gere, J.M. Analysis of shear cores using super elements. *J. Struct. Div.* **1976**, *102*, 267–283. [CrossRef]
9. Luo, Z.H.; Wu, J.S. Review on research of structural system with suspended vibration reduction. *J. Tianjin Ins. Urb. Con.* **2001**, *7*, 14–17.
10. Luo, Z.H. The Earthquake Response of High-Rise Suspended Structure. *J. Tianjin Ins. Urb. Constr.* **1996**, *2*, 6–12.
11. Zhang, Y.C.; Liu, J.H.; Chou, C.Y. The Structural Design and Construction of Kaohsiung Publ is Library Suspension Structure. *Pro. Steel Build. Struct.* **2016**, *18*, 57–71.
12. Chen, J.X.; Bao, L.J.; Hu, Z.Q.; Xie, Y.C.; Cui, F.C.; Liu, C. Suspension structure design of Jinqiao Guopei Center. *Build. Struct.* **2022**, *52*, 42–47+103.
13. Wang, X.F.; Lin, C.W.; Xu, B.; Li, K.L.; Lei, T.; Xiong, L. Research on structural system of Guiyang 201 Building. *Build. Struct.* **2012**, *42*, 10–14+28.
14. Tang, X.H. Design and analysis of the suspension structure of a dish-shaped air exhibition hall. *Build. Struct.* **2022**, *52*, 270–275.
15. Zhang, S.G. Design of a Brace Transferring Truss Suspended Structure. *Struct. Eng.* **2013**, *29*, 38–43.
16. Yao, Y.L.; Zhang, Y.J.; Zhang, Y.L.; Qu, H.N. Seismic Performance of Composite Suspension Structure in Industrial Construction. *Earthq. Res. Eng. Retrofit.* **2014**, *36*, 56–60+49.
17. Yan, X.X.; Hu, D.M.; Qi, X.M. Structural design of gad Enterprise Building. *Build. Struct.* **2017**, *47*, 1–8.
18. Zeng, B.; Zhang, M.B.; Lu, Z.T. Research on stress performance of a new type of flexible suspension tension structure. *China Civ. Eng. J.* **2010**, *43*, 28–33.
19. Han, J.W. Application and Performance of Mixed Hanging Structure in Long-Span Architecture. Master's Thesis, Harbin Institute of Technology, Harbin, China, 2014.
20. Algirdas, J.; Alfonsas, D.N.; Leonas, U. Non-Linear Behaviour and Analysis of Innovative Suspension Steel Roof Structures. *Buildings* **2024**, *14*, 661. [CrossRef]
21. Guo, Y.L.; Dou, C. Design theory and Chinese Technical Specification for Steel arch Structure. *Steel Constr.* **2009**, *24*, 59–70.
22. José, L.M.J.; Ignacio, H.S.B. Non-linear plastic analysis of steel arches under lateral buckling. *J. Constr. Steel Res.* **2011**, *67*, 1850–1863. [CrossRef]
23. Spoorenberg, R.C.; Snijder, H.H.; Hoenderkamp, J.C.D. A theoretical method for calculating the collapse load of steel circular arches. *Eng. Struct.* **2012**, *38*, 89–103. [CrossRef]
24. Cheng, P. In-Plane Nonlinear Theory and Elastic-Plastic Stability of Pined Circular Arches. Master's Thesis, Zhe jiang University, Hangzhou, China, 2005.
25. Zhang, Z.Y. Research on the Expression of Arch Structure in Long Soan Buildings. Ph.D. Thesis, Harbin Institute of Technology, Harbin, China, 2009.
26. Lu, J. Brief Introduction on Design of Special- Shaped Steel Structure Arch Bridge. *Urb. Rd. Bri. Flood Control.* **2019**, *5*, 139–141+158.
27. He, B.W.; Deng, C.G.; Gong, J.S. Stress and Ultimate Carrying Capacity Research of Abutment of through Tied Bar Steel Arch-bridge. *Sci. Tech. Eng.* **2020**, *20*, 12112–12117.
28. Krishna, P.; Agrawal, T.P. *Cable-Suported Roof*; McGaw-Hill: Kingsport, TN, USA; New York, NY, USA, 1978.
29. Zhang, Y.W.; Shen, S.Z. Study of Hypar Cable-Arch Mixed System. *J. HarBin Univ. Civ. Eng Arch.* **1986**, *1*, 1–17.
30. Li, L.L.; Han, J.W. Form and Application of Arch Hanging Structure in Long-Span Sport Architecture. *Urb. Arch.* **2014**, *9*, 116–118.
31. Liu, H.B. *Midas Gen Software Basics and Examples Tutorial*; Tianjin University Press: Tianjin, China, 2020.
32. *GB 50017-2017*; Steel Structure Design Standard. SAC (Standardization Administration of the People's Republic of China): Beijing, China, 2018.
33. Buitrago, M.; Sagaseta, J.; Adam, J.M. Effects of Sudden Failure of Shoring Elements in Concrete Building Structures under Construction. *Eng. Struct.* **2018**, *172*, 508–522. [CrossRef]
34. Wang, D.; Ju, R.B.; Mu, F.C.; Wang, C. Construction of Large-span Suspended Steel Structure and Application of Temporary Support. *Technol. Cons. Tech.* **2025**, *54*, 82–87.
35. Abaqus Inc. *Abaqus Analysis User's Manual*; Dassault Systèmes: Paris, France, 2015.
36. Zhang, Y.C.; Zhou, S.H. *Structural Steel Design Principle*; Higher Education Press: Beijing, China, 2020.

Disclaimer/Publisher's Note: The statements, opinions and data contained in all publications are solely those of the individual author(s) and contributor(s) and not of MDPI and/or the editor(s). MDPI and/or the editor(s) disclaim responsibility for any injury to people or property resulting from any ideas, methods, instructions or products referred to in the content.